A level-set-based topology optimization strategy using radial basis functions and a Hilbertian velocity extension

Giovanna C. Andrade[1] and Sandra A. Santos[1]

[1]*Institute of Mathematics, University of Campinas, Rua Sergio Buarque de Holanda, 651, 13083-859, Campinas, São Paulo, Brazil*
Emails: `giovanna.castelloa@gmail.com`, `sandra@ime.unicamp.br`

June 15, 2022

Abstract

This work addresses the structural compliance minimization problem through a level-set-based strategy that rests upon radial basis functions with compact support combined with Hilbertian velocity extensions. A consistent augmented Lagrangian scheme is adopted to handle the volume constraint. The linear elasticity model and the variational problem associated with the computation of the velocity field are tackled by the finite element method using resources from the FEniCS project. The parameterization mesh constituted by the centers of the radial basis functions may be decoupled from the finite element mesh. A numerical investigation is conducted employing a Python implementation and five benchmark structures. Aimed at isolating the distinct aspects that compose the proposed strategy, the experiments provide grounds to analyze and put into perspective the inherent decisions and the related elements.

Keywords: Topology optimization, Level-set method, Radial basis function, Hilbertian velocity extension, Shape derivatives

AMS Classification: 74B05, 74P05, 74S05, 70H20, 65D12

1 Introduction

Structural topology optimization, a challenging stage of the design of structures, has been receiving significant attention in the last decades, with important recent advances [12, 30, 40]. The minimization of the mean compliance of a static structure, subject to a volume constraint upon the available material is a benchmark problem in this field. The goal is to attain the stiffest structure that fits into a given domain, satisfying external loads and boundary conditions, with a prescribed maximum volume. Aimed at modeling moving boundaries [25, 28, 23], the level set methods started to be considered for tackling such topology optimization problems in the late '90s as an alternative to the density-based homogenization methods [32].

Three general features distinguish the level-set topology optimization methods: the parameterization of the level-set function; the mechanical model, and the optimization strategy. Radial-based functions (RBF) have been used to define smooth parameterizations for the level-set function [35, 36, 37], and this is the choice of this work, specifically through the compact support Wendland functions [38]. When it comes to the mechanical model, the geometry mapping is based on the Ersatz material distribution within the finite element analysis, under the linear elasticity regime. As regards the optimization strategy, the Hilbertian extension is used to update the sensitivities [11, 15], in contrast with the natural extension of the velocities, used in [35, 36, 37] together with the RBF parameterization. As remarked by de Gournay in [11], the expectation is twofold: achieving a strategy less dependent on the mesh, and producing a velocity field more regular than the one obtained by the natural extension. Moreover, instead of just keeping a constant value for the Lagrange multiplier (see e.g. [11, 15]), or resting upon a relaxation procedure for updating the volume constraint, as in [36], we have adopted an augmented Lagrangian scheme with a consistent updating of the related elements [4] based on the shape derivative of the cost functional. Challis [7] also worked with an augmented Lagrangian functional, with the underlying constraint being of equality type, and instead of the parameterized approach, she considered the conventional level-set method based on the Hamilton-Jacobi partial differential equation. It is worth noticing that, although in [36] the augmented Lagrangian is somehow used, the shape derivative is not aligned with such a function. Additionally, in the current work, the finite element mesh for the discretized structural model is assumed to be decoupled from the parameterization mesh, to keep the optimization process efficiency while maintaining the accuracy of the predicted structural responses [32, 37]. In [35, 36, 37], the RBF centers are set exactly as the finite element nodes. Recently, the work [21] employs compactly supported radial basis functions combined with a shape sensitivity constraint factor to control the step length within the method of the moving asymptotes, whereas the robust topology optimization method of [33] uses RBF and a gradient-based optimization algorithm resting upon the shape derivative principle to compute the related sensitivities.

Our numerical experiments were planned aiming to isolate and systematically analyze the effect of the different aspects that compose the presented strategy. Such a goal is known to be a challenge in structural topology optimization considering the great number of parameters and approximations involved, especially when regularization procedures are adopted [32]. The primary motivation of this research came from designing a sound strategy, properly setting the associate parameters, and handling the updates. These tasks, in turn, created our main difficulties, mostly involving the convergence of the generated sequence of approximations. The oscillatory satisfaction of the volume constraint, for example, provided valuable feedback

for adjusting the choices, driving us to establish a setting as consistent as possible.

The roadmap of this work is as follows. Section 2 contains the continuous problem formulation, and the associate augmented Lagrangian. Section 3 briefly describes the conventional level-set method. Section 4 presents the necessary elements to compute descent directions using the Hilbertian extension. Section 5 provides the ingredients to establish the RBF parameterized level-set topology optimization algorithm. Section 6 is dedicated to the numerical experiments. Section 7 concludes the work, indicating prospective ideas for future investigation.

2 Problem formulation

2.1 The continuous formulation of the minimum compliance problem

The structures considered in this work are assumed to be under *plane stress state* and therefore can be treated as two-dimensional [27]. As we are interested in determining the optimum topology and geometry of a structure, the optimization variable of the problem is a set of $\mathbb{R}^2$. Given a *reference domain* $\mathcal{D} = [0, l_x] \times [0, l_y] \subset \mathbb{R}^2$, let $\mathcal{P}(\mathcal{D})$ be the set of its subsets. Each considered *design domain* is a set $\Omega \in \mathcal{P}(\mathcal{D})$, assumed to be in *static equilibrium*. Boundary conditions such as the external traction and support region are defined for the reference and the design domain, as illustrated in Figure 1, and described as follows. The boundary of the reference domain $\partial\mathcal{D}$ is divided in three disjoints parts: $\partial\mathcal{D} = \partial\mathcal{D}_D \cup \partial\mathcal{D}_N \cup \partial D_0$, in which $\partial\mathcal{D}_D$ refers to the homogeneous Dirichlet condition; $\partial\mathcal{D}_N$ denotes the non-homogeneous Neumann condition, and $\partial\mathcal{D}_0$ represents the homogeneous Neumann condition. Concerning the boundary $\partial\Omega$, we have $\partial\Omega = \Gamma_D \cup \Gamma_N$, with $\Gamma_D \subset \partial D_D$ and $\Gamma_N = \Gamma_0 \cup \partial\mathcal{D}_N$.
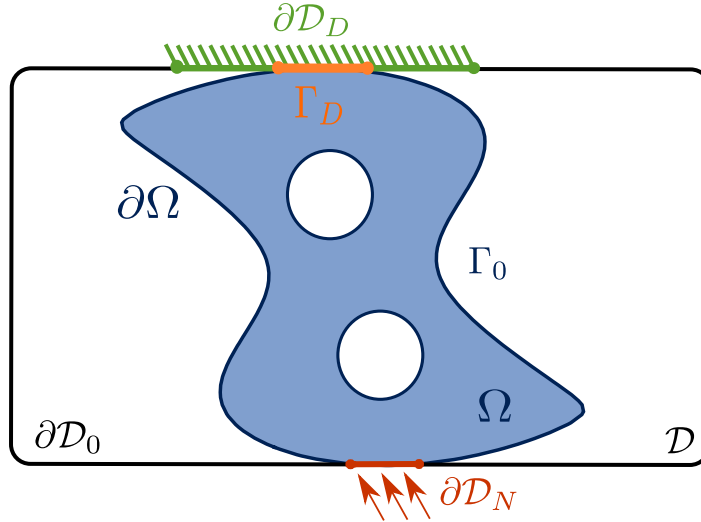

Figure 1: Reference domain $\mathcal{D}$, together with an example of design domain $\Omega \in \mathcal{P}(\mathcal{D})$ and the associated boundary conditions.

The static equilibrium state is formulated as the following boundary value problem

$$
\begin{cases}
\nabla \cdot \boldsymbol{\sigma}(\boldsymbol{x}) = -\boldsymbol{f}, & \boldsymbol{x} \in \Omega, \\
\boldsymbol{u}(\boldsymbol{x}) = 0, & \boldsymbol{x} \in \Gamma_D, \\
\sigma(\boldsymbol{x}) \cdot \widehat{\boldsymbol{n}} = \boldsymbol{g}, & \boldsymbol{x} \in \Gamma_N,
\end{cases}
\tag{1}
$$

where $\boldsymbol{u}$ denotes the *displacement vector*, and $\boldsymbol{\sigma}(\boldsymbol{x}) := Ae(\boldsymbol{u})$ represents the *stress*, being A the *material stiffness tensor*, and $e(\boldsymbol{u}) := \left(\mathrm{J}_{\boldsymbol{u}} + \mathrm{J}_{\boldsymbol{u}}^\intercal\right)/2$ the *linearized strain*, with Jacobian $\mathrm{J}_{\boldsymbol{u}}$. The outward unit normal vector to Ω is indicated by $\widehat{\boldsymbol{n}}$. In specific, we consider structures built with isotropic materials, so that the fourth order tensor A can be expressed in terms of the *Lamé constants* μ and λ as $\boldsymbol{\sigma}(\boldsymbol{x}) = \mu e(\boldsymbol{u}) + \lambda \nabla \cdot \boldsymbol{u} I$. This problem is addressed by *finite element analysis* and therefore it is convenient to rewrite (1) in variational form. Let $\mathbb{V} := \left\{ \boldsymbol{v} \in (\mathbb{H}^1(\Omega))^2 : \boldsymbol{v} = 0 \text{ em } \Gamma_D \right\}$ be the set of admissible displacements. Following [8], problem (1) can be expressed as finding $\boldsymbol{u} \in \mathbb{V}$ that satisfies

$$
a(\boldsymbol{u}, \boldsymbol{v}) = l(\boldsymbol{v}), \quad \forall \ \boldsymbol{v} \in \mathbb{V},
\tag{2}
$$

with $a : \mathbb{V} \times \mathbb{V} \to \mathbb{R}$ and $l : \mathbb{V} \to \mathbb{R}$ defined as

$$
a(\boldsymbol{u}, \boldsymbol{v}) := \int_\Omega A\ e(\boldsymbol{u}) : e(\boldsymbol{v})\ d\boldsymbol{x}, \quad \text{and} \quad l(\boldsymbol{v}) := \int_\Omega \boldsymbol{f} \cdot \boldsymbol{v}\ d\boldsymbol{x} + \int_{\Gamma_N} \boldsymbol{g} \cdot \boldsymbol{v}\ ds.
\tag{3}
$$

The solution $\boldsymbol{u}$ of this boundary value problem is the displacement suffered by the structure once submitted to the given conditions. Once $\boldsymbol{u}$ has been obtained, the *compliance* of the structure is defined as $J(\Omega) := a(\boldsymbol{u}, \boldsymbol{u}) \overset{(2)}{=} l(\boldsymbol{u})$. Hence, the optimization problem upon consideration may be formulated as

$$
\min_{\Omega \in \mathcal{P}(\mathcal{D})} J(\Omega) \ \text{ subject to } \ \mathcal{C}(\Omega) \leq 0,
\tag{4}
$$

in which, given a prescribed volume fraction $\overline{V}$, the volume constraint is stated as

$$
\mathcal{C}(\Omega) := V(\Omega) - \overline{V}, \quad \text{with } V(\Omega) := \frac{1}{l_x l_y} \int_\Omega d\boldsymbol{x}.
$$

It is worth noticing that the static equilibrium is primarily imposed through the finite element analysis for each generated structure so that just the volume restriction is treated as a constraint. Moreover, the requirement $\Omega \in \mathcal{P}(\mathcal{D})$ is ensured by the implicit representation of the domain provided by the level-set strategy, as detailed in Section 3.

Assuming the region $\mathcal{D} \setminus \Omega$ to be filled with elastic material described by the tensor εA, being $\varepsilon > 0$ a small constant, problem (1) may be extended to the reference domain $\mathcal{D}$ [15, 2], in the so-called Ersatz material approach. Hence, Hooke's law may be stated in $\mathcal{D}$ as

$$
A_\Omega := A \mathcal{X}_\Omega + \varepsilon A \mathcal{X}_{\mathcal{D} \setminus \Omega}
\tag{5}
$$

where $\mathcal{X}_\Omega$ denotes the indicator function of the set Ω. As a result, although the optimization is performed with respect to the variable set Ω, such a set is embedded in the reference domain $\mathcal{D}$.

2.2 The augmented Lagrangian formulation

In this work, we employ an augmented Lagrangian scheme to address problem (4), based on the Powell-Hestenes-Rockafellar augmented Lagrangian function (cf. [4] and references therein). The related functional is given by

$$\mathcal{L}_\rho(\Omega, \Lambda) := J(\Omega) + \frac{\rho}{2}\left(\max\left\{0, \mathcal{C}(\Omega) + \frac{\Lambda}{\rho}\right\}^2 - \frac{\Lambda^2}{\rho^2}\right), \tag{6}$$

in which $\Lambda \in \mathbb{R}_+$ denotes the Lagrange multiplier and $\rho > 0$ is the penalty parameter. By consistently updating the sequences $\{\Lambda_k\}$ and $\{\rho_k\}$, $k \in \mathbb{N}$, unconstrained problems as follows should be considered

$$\underset{\Omega \in \mathcal{P}(\mathcal{D})}{\text{minimize}}\ \mathcal{L}_{\rho_k}(\Omega, \Lambda_k). \tag{7}$$

More specifically, given the parameters $\tau \in [0, 1]$, $\gamma > 1$, $\rho_{\max}$ and the initial values Λ_0 and ρ_0, at the k-th iteration, denoting by Ω_k a stationary point of problem (7), the infeasibility measure is defined by $\mathcal{V}^k := \max\{C(\Omega_k), -\Lambda_k/\rho_k\}$, so that the Lagrange multiplier is updated by

$$\Lambda_{k+1} = \max\{\Lambda_k + \rho_k C(\Omega_k), 0\}, \tag{8}$$

and the penalty parameter obeys

$$\text{if}\ \ |\mathcal{V}^k| < \tau|\mathcal{V}^{k-1}|\ \ \text{then}\ \ \rho_{k+1} = \rho_k,\ \ \text{otherwise}\ \ \rho_{k+1} = \min\{\gamma\rho_k, \rho_{\max}\}. \tag{9}$$

3 The conventional level-set method

In contrast with methods that rely on an explicit parameterization of the design domain, in level-set methods, the geometry and topology are represented implicitly as the zero level set of a higher dimensional function, as illustrated in Figure 2. According with [24], such methods are characterized when dynamics is added to the level-set function by allowing it to vary along a fictitious time. Defining the *level set function* (LSF) by $\phi : \mathcal{D} \times \mathbb{R}_+ \mapsto \mathbb{R}$, we will assume the following convention

$$\begin{cases} \phi(\boldsymbol{x}, t) > 0 \iff \boldsymbol{x} \in \Omega \cap \mathcal{D}, \\ \phi(\boldsymbol{x}, t) = 0 \iff \boldsymbol{x} \in \partial\Omega \cap \mathcal{D}, \\ \phi(\boldsymbol{x}, t) < 0 \iff \boldsymbol{x} \in \mathcal{D}\backslash(\Omega \cup \partial\Omega). \end{cases} \tag{10}$$

Therefore, for fixed t, the domain Ω_t and its boundary $\partial\Omega_t$ are stated as $\Omega_t := \{\boldsymbol{x} \in \mathcal{D} : \phi(\boldsymbol{x}, t) > 0\}$ and $\partial\Omega_t := \{\boldsymbol{x} \in \mathcal{D} : \phi(\boldsymbol{x}, t) = 0\}$, respectively. Assuming that $\partial\Omega_t$ can be parameterized as a curve $\boldsymbol{x}(t)$, then this curve satisfies $\phi(\boldsymbol{x}(t), t) = 0$. The boundary movement can thus be obtained by taking the derivative with respect to t, which by the chain rule leads to the *Hamilton-Jacobi* (HJ) equation

$$\partial_t\phi(\boldsymbol{x}(t), t) + \boldsymbol{v}^\circ(\boldsymbol{x}(t), t) \cdot \nabla\phi(\boldsymbol{x}(t), t) = 0, \quad \text{for}\ (\boldsymbol{x}(t), t)\ \text{in}\ \partial\Omega_t \times \mathbb{R}_+. \tag{11}$$

The term $\boldsymbol{v}^\circ(\boldsymbol{x}(t), t) := \boldsymbol{x}'(t)$ denotes the boundary velocity field. Furthermore, if v_n° and v_t° respectively denote the normal and the tangential components of this field then, since the unit outward normal vector to $\partial\Omega_t$ can be written as $\widehat{\boldsymbol{n}} = -\nabla\phi/\|\nabla\phi\|$ and $\widehat{\boldsymbol{t}}$ and $\nabla\phi$ are
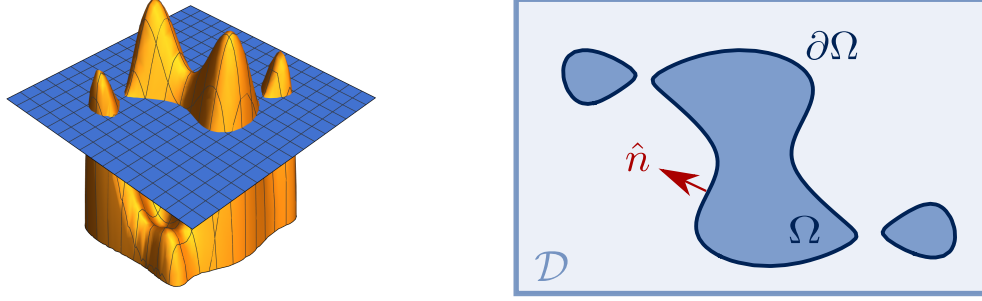
Figure 2: The LSF graph (left), and the implicit representation of the design domain Ω (right).

orthogonal, we obtain an equivalent expression that involves only the normal component of the field

$$\partial_t \phi(\boldsymbol{x}(t), t) - \upsilon_n^\circ(\boldsymbol{x}(t), t) \|\nabla \phi(\boldsymbol{x}(t), t)\| = 0, \quad \text{for } (\boldsymbol{x}(t), t) \text{ in } \partial\Omega_t \times \mathbb{R}_+. \quad (12)$$

If the velocity field or its normal component are extended to the reference domain (respectively denoted by $\boldsymbol{v}$ or υ_n), then equations (11) and (12) may be written for all $\boldsymbol{x}$ in $\mathcal{D}$ and can be used to update the level-set equation and, consequently, the design domain. This characterizes *conventional level-set methods* and finite-difference schemes such as upwind differencing can be used for solving the partial differential equation (PDE) and updating the nodal values of the LSF [15, 24, 7]. Modified evolution equations may also be considered to stabilize numerical solutions, regularize the LSF and nucleate new holes [32, 7, 26, 39]. On the *parameterized level set method* adopted here, the LSF is considered to be a linear combination of spatially fixed basis functions and the original PDE is converted in a system of ordinary differential equations (ODE's). In particular, the following modified Hamilton-Jacobi equation is adopted

$$\partial_t \phi(\boldsymbol{x}, t) - \upsilon_n(\boldsymbol{x}, t)\delta(\phi(\boldsymbol{x}, t)) = 0, \quad \text{for } (\boldsymbol{x}, t) \text{ in } \mathcal{D} \times \mathbb{R}_+, \quad (13)$$

in which

$$\delta(\phi) = \begin{cases} 0 & \text{if } \phi < -\Delta \text{ or } \phi > \Delta \\ \frac{1}{2\Delta}\left(1 + \cos\left(\frac{\pi\phi}{\Delta}\right)\right) & \text{if } -\Delta \leq \phi \leq \Delta, \end{cases} \quad (14)$$

is an approximate delta function and the parameter Δ has the magnitude of $\max|\phi|$. This scheme aims to avoid the unbounded growth of the LSF [36, 37, 39]. We will come back to this matter in Section 5, after providing the details concerning the velocity extension.

4 Descent directions by the Hilbertian velocity extension

Choosing the velocity field and extending it appropriately are key points for the optimization scheme since the motion of the level-set function should be driven towards a minimizer of the cost functional. In finite dimension, the *steepest descent direction* [22] is a classical way of obtaining a descent direction from (minus) the gradient of the cost function. An analogous

approach can be considered by taking the shape derivative of the cost functional (6), usually defined through its Eulerian semi derivative (cf. [31, Definition 2.19]).

Following [2], let us denote as $d\mathcal{L}_\rho(\Omega, \Lambda; \boldsymbol{\theta})$ the shape derivative of $\mathcal{L}_\rho$ along the direction $\boldsymbol{\theta} \in W^{1,\infty}(\mathbb{R}^2, \mathbb{R}^2)$. Since this differential operator is linear and the chain rule applies [19, §7.3], the *boundary expression* for the shape derivative of (6) can then be computed based on $dJ(\Omega, \boldsymbol{\theta})$ [2, Theorem 7] and $dV(\Omega, \boldsymbol{\theta})$ [2, Remark 6], and results in

$$d\mathcal{L}_\rho^{\text{SURF}}(\Omega, \Lambda; \boldsymbol{\theta}) = \int_{\Gamma_0} \mathcal{G}\boldsymbol{\theta} \cdot \widehat{\boldsymbol{n}} ds, \tag{15}$$

with $\mathcal{G} := -Ae(\boldsymbol{u}) : e(\boldsymbol{u}) + \frac{\rho}{l_x l_y} \max\{0, \mathcal{C}(\Omega) + \frac{\Lambda}{\rho}\}$. This expression agrees with the Hadamard-Zolésio structure theorem, a fundamental result in shape optimization [13, p. 480-481]. Consequently, $v_n^\circ = -\mathcal{G}$ is an immediate choice of descent velocity field on $\partial\Omega$. Furthermore, due to the Ersatz material approach, $\mathcal{G}$ is defined on the whole reference domain, so that the choice $v_n = -\mathcal{G}$ is a possible extension approach, known as *natural extension method* and widely adopted in structural optimization, cf. [35, 36, 37, 7].

Since the adopted evolution scheme requires only the normal component of the field $\boldsymbol{v}$ (cf. (12)), we consider the *Hilbertian extension* approach proposed by de Gournay [11], which consists in solving the scalar variational problem of finding $\theta \in \mathbb{H}^1(\mathcal{D})$ that satisfies

$$\langle \theta, \beta \rangle_{\mathbb{H}^1(\mathcal{D})} = -d\mathcal{L}_\rho(\Omega, \Lambda; \beta\widehat{\boldsymbol{n}}), \ \forall \beta \in \mathbb{H}^1(\mathcal{D}), \tag{16}$$

where

$$\langle \theta, \beta \rangle_{\mathbb{H}^1(\mathcal{D})} := \int_{\mathcal{D}} \left(a^2 \nabla\theta \cdot \nabla\beta + \theta \, \beta \right) d\boldsymbol{x}, \tag{17}$$

being $\langle \cdot, \cdot \rangle_{\mathbb{H}^1(\mathcal{D})}$ an inner product on $\mathbb{H}^1(\mathcal{D})$ and $a \in \mathbb{R} \setminus \{0\}$ the *extension-regularization parameter*. Because from (16), $d\mathcal{L}_\rho(\Omega, \Lambda, \theta\widehat{\boldsymbol{n}}) = -\langle \theta, \theta \rangle_{\mathbb{H}^1(\mathcal{D})} < 0$, it follows that $v_n = \theta$ ensures local decreasing of $\mathcal{L}_\rho$.

As shown in [11], this approach results in a more regular velocity field than the one defined by the *natural extension method*, considered by Wei et al. [36]. Our choice is also facilitated by the FEniCS resources [18], and it is similar to Laurain's work [15], which considered the distributed expression of the shape derivative, working with the extension of (11) to $\mathcal{D}$ instead of (12).

Denoting the Jacobian matrix of the vector valued function $\boldsymbol{\theta}$ by $J_{\boldsymbol{\theta}}$, the *volume (or distributed) expression* for the shape derivative of (6) is assembled from the components

$$dJ^{\text{VOL}}(\Omega; \boldsymbol{\theta}) = \int_{\mathcal{D}} \left(2J_{\boldsymbol{\theta}}^T A_\Omega e(\boldsymbol{u}) - A_\Omega e(\boldsymbol{u}) : e(\boldsymbol{u})I \right) : J_{\boldsymbol{\theta}} \, d\boldsymbol{x} \tag{18}$$

$$\text{and} \quad dV^{\text{VOL}}(\Omega, \boldsymbol{\theta}) = \int_{\mathcal{D}} I : J_{\boldsymbol{\theta}} \, d\boldsymbol{x}, \tag{19}$$

reaching the following expression

$$d\mathcal{L}_\rho^{\text{VOL}}(\Omega, \Lambda; \boldsymbol{\theta}) = dJ^{\text{VOL}}(\Omega, \boldsymbol{\theta}) + \frac{\rho}{l_x l_y} \max\left\{ 0, \mathcal{C}(\Omega) + \frac{\Lambda}{\rho} \right\} dV^{\text{VOL}}(\Omega, \boldsymbol{\theta}). \tag{20}$$

In this case, the variational problem to be solved is to find $\boldsymbol{\theta} \in \mathbb{H}^1(\mathcal{D})^2 := \mathbb{H}^1(\mathcal{D}) \times \mathbb{H}^1(\mathcal{D})$ satisfying

$$\langle \boldsymbol{\theta}, \boldsymbol{\beta} \rangle_{\mathbb{H}^1(\mathcal{D})^2} = -d\mathcal{L}_\rho^{\text{VOL}}(\Omega, \Lambda; \boldsymbol{\beta}), \ \forall \boldsymbol{\beta} \in \mathbb{H}^1(\mathcal{D})^2, \tag{21}$$

in which

$$\langle \boldsymbol{\theta}, \boldsymbol{\beta} \rangle_{\mathbb{H}^1(\mathcal{D})^2} := \int_{\mathcal{D}} \left(a^2 \nabla \boldsymbol{\theta} : \nabla \boldsymbol{\beta} + \boldsymbol{\theta} \cdot \boldsymbol{\beta} \right) \, d\boldsymbol{x}. \tag{22}$$

In contrast with (15), the distributed expression (20) considers both weak and strong phases of the Ersatz approach so that its use is consistent with any multiphase problem. The practical impact of the usage of (15) against (20) to obtain the velocity extension is addressed in the experiment of Subsection 6.5. For further discussions on extension procedures, see e.g. the review article of Dijk et al. [32].

5   The parameterized level-set method using radial-basis functions

As the driving force for the parameterized level-set method, we have adopted the radial-basis functions (RBFs). Two fundamental procedures must be defined, namely the *initialization* of the parameters, and their *evolution*, for which we have followed the lines of [35, 36, 37], summarized next.

Let $\Sigma = \{\boldsymbol{\xi}^{(i)} = (x_1^{(i)}, x_2^{(i)}), i = 1, \ldots, n_R\} \subset \mathcal{D}$ be a discretization of the reference domain, and denote by $\mathcal{R}(\|\boldsymbol{x} - \boldsymbol{\xi}^{(i)}\|)$ an RBF centered at $\boldsymbol{\xi}^{(i)}$. Assuming that the basis functions are fixed during the evolution process, the *parameterized level set function* (PLSF) is defined as $s : \mathcal{D} \times \mathbb{R}^+ \mapsto \mathbb{R}$ such that

$$s(\boldsymbol{x}, t) = \boldsymbol{r}_\Sigma(\boldsymbol{x})^\mathsf{T} \boldsymbol{\alpha}(t) = \sum_{i=1}^{n_R} \mathcal{R}(\|\boldsymbol{x} - \boldsymbol{\xi}^{(i)}\|) \alpha_i(t). \tag{23}$$

For the parameters *initialization*, we assume that the nodal values ϕ_i of the PLSF are known at each point $\boldsymbol{\xi}^{(i)}$. Then, $\boldsymbol{\alpha}^{(0)}$ is the solution of the interpolation problem $s(\boldsymbol{\xi}^{(i)}) = \phi_i$ for $i = 1, \ldots, n_R$. In matrix form, this can be expressed as $\boldsymbol{G}\boldsymbol{\alpha} = \Phi$, in which $g_{ij} = \mathcal{R}(\|\boldsymbol{\xi}^{(i)} - \boldsymbol{\xi}^{(j)}\|)$, $i, j = 1, \ldots, n_R$ and $\Phi = (\phi_1, \ldots, \phi_{n_R})^\mathsf{T}$. Nonsingularity of the matrix $\boldsymbol{G}$ depends on the type of RBF chosen. In [36], the authors work mainly with *multiquadrics* (MQ), for which a first-degree polynomial term is added to (23) to ensure positive definiteness [5]. Here we consider *C2-Wendland's compactly supported* (CS) RBF, defined as

$$\mathcal{R}^{\mathsf{CS}}(\|\boldsymbol{x} - \boldsymbol{\xi}\|) := (\max\{0, 1 - r_{\boldsymbol{\xi}}(\boldsymbol{x})\})^4 (4 r_{\boldsymbol{\xi}}(\boldsymbol{x}) + 1), \tag{24}$$

with

$$r_{\boldsymbol{\xi}}(\boldsymbol{x}) := \tfrac{1}{d_{sp}} \sqrt{\|\boldsymbol{x} - \boldsymbol{\xi}\|^2 + c^2}, \tag{25}$$

where c is a small shape parameter and d_{sp} is the radius of support. In contrast with multiquadric RBF, this choice leads to banded interpolation matrices with bandwidth depending directly on d_{sp}, as shown in Figure 3.

To address the *evolution* of the PLSF, we may evaluate expression (23) by (13), which results in

$$\boldsymbol{r}_\Sigma(\boldsymbol{x})^\mathsf{T} \boldsymbol{\alpha}'(t) - \upsilon_n(\boldsymbol{x}, t) \, \delta(\phi(\boldsymbol{x}, t)) = 0. \tag{26}$$

By evaluating this expression in each knot $\boldsymbol{\xi}^{(j)}$, $j \in \{1, \ldots, n_R\}$, which can be considered a collocation formulation of the general method of lines [35], we obtain a set of n_R ODE's on t which can be written in matrix form as

$$\boldsymbol{G}\boldsymbol{\alpha}'(t) = \boldsymbol{B}(\boldsymbol{\alpha}, t)$$
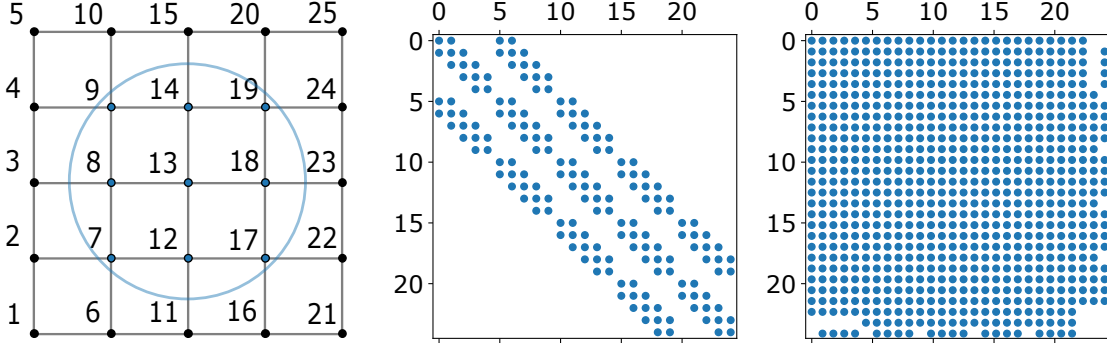
Figure 3: Example with a 4×4 square mesh (left) and the structure of the interpolation matrices associated, respectively, with a CS-RBF with $d_{sp} = 1.5\Delta x$ (where Δx is the element size) – (center) and an MQ-RBF (right).

by defining the components of the right-hand side vector as

$$B_j(\boldsymbol{\alpha}, t) = v_n(\boldsymbol{\xi}^{(j)}, t)\, \delta\left(\boldsymbol{r}_\Sigma(\boldsymbol{\xi}^{(j)})^\mathsf{T} \boldsymbol{\alpha}(t)\right), \quad j = 1, \ldots, n_R. \tag{27}$$

This ODE system can be solved using a first-order forward Euler's method, which gives

$$\boldsymbol{\alpha}^{(k+1)} = \boldsymbol{\alpha}^{(k)} + \Delta t \boldsymbol{G}^{-1} \boldsymbol{B}(\boldsymbol{\alpha}^{(k)}, t_k). \tag{28}$$

This means that for each evolution step, a linear system involving $\boldsymbol{G}$ must be solved, and therefore, the sparsity inherent in the CS-RBFs is valuable for saving computational effort. Moreover, since the knots are fixed, this matrix is constant and the related computational linear algebra can be efficiently explored.

Analogous versions of equations (26), (27) and (28) can be obtained by evaluating (23) in different evolution equations. This is the case, for example, of equation (11), which will be considered in association with the *distributed expression* of shape derivative in Subsection 6.5. In [35], the authors consider the development with equation (12).

The flow chart of the proposed algorithm is presented in Figure 4. At each iteration, the domain that is implicitly represented by the LSF must be mapped onto the finite element mesh, used in the structural analysis, the evaluation of the objective function, and the Hilbertian extension problem. Based on definition (10), the geometry mapping strategy adopted on this paper rests upon a smooth interface between the weak and the strong phases of the material Ersatz approach [36, 32]. For this matter, we define $H_\varepsilon(\phi) := (1 - \varepsilon)H(\phi) + \varepsilon$, in which

$$H(\phi) := \begin{cases} 0, & \text{if } \phi < -\Delta, \\ \frac{1}{2} + \frac{\phi}{2\Delta} + \frac{1}{2\pi}\sin(\frac{\pi\phi}{\Delta}), & \text{if } -\Delta \le \phi \le \Delta, \\ 1, & \text{if } \phi > \Delta \end{cases} \tag{29}$$

denotes an approximate Heaviside function and $\delta_\varepsilon = H'_\varepsilon(\phi)$. Then, integration on the domain and at its boundary can be expressed based on $\int_\Omega f_1\, d\boldsymbol{x} = \int_D f_1 H_\varepsilon(\phi)\, d\boldsymbol{x}$ and $\int_{\partial\Omega} f_2\, ds = \int_D f_2\, \delta_\varepsilon(\phi)\, d\boldsymbol{x}$, being f_1, f_2 arbitrary functions [24].

9

```
┌─────────────────────────────────────────┐
│        Parameters initialization         │
└─────────────────────────────────────────┘
                    ↓
┌─────────────────────────────────────────┐
│  Solution of interpolation problem for initial α  │
└─────────────────────────────────────────┘
                    ↓
┌─────────────────────────────────────────┐
│        Geometry mapping onto Ξ           │
└─────────────────────────────────────────┘
                    ↓
┌─────────────────────────────────────────┐
│      Structural analysis and evaluation  │
│          of the objective function       │
└─────────────────────────────────────────┘
                    ↓
         If convergence, stop. Otherwise
                    ↓
┌─────────────────────────────────────────┐
│     Obtaining and extending a velocity field │
│   onto Ξ (Hilbertian or natural extension)   │
└─────────────────────────────────────────┘
                    ↓
┌─────────────────────────────────────────┐
│        Updating of coefficients α        │
└─────────────────────────────────────────┘
                    ↓
┌─────────────────────────────────────────┐
│  Updating of augmented Lagrangian parameters  │
└─────────────────────────────────────────┘
```
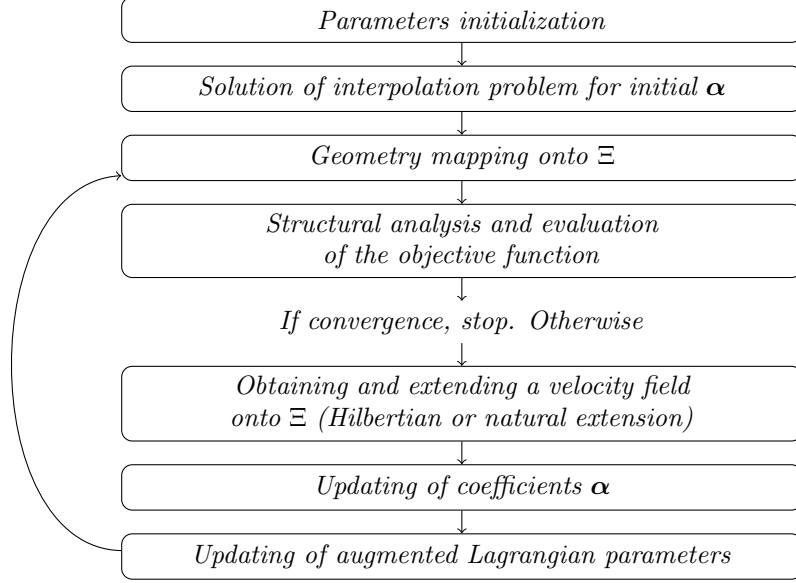
Figure 4: Flow chart of the proposed parameterized level-set-based topology optimization algorithm.

For the numerical implementation of parameterized level set approaches, it may be convenient to set the nodes of the finite element mesh exactly as the set Σ of the centers of the basis functions, as adopted by [35, 36]. On the other hand, it is known that the spatial resolution of the discretized structural model must be large enough to meet the desired accuracy of the predicted responses of the finite element analysis, whereas a large number of basis functions leads to large linear systems for the design update [32]. Therefore, as long as a proper mapping between Σ and the finite element knots is defined, both meshes can be decoupled.

By stating the finite element mesh used to represent the structure as $\Xi := \{\widetilde{\boldsymbol{\xi}}^{(i)} = (\widetilde{x}_1^{(i)}, \widetilde{x}_2^{(i)}), i = 1, \ldots, n_S\}$, and evaluating (23) for each point of Ξ, the nodal values of the LSF can be obtained straightforwardly from $\boldsymbol{s}^\Xi = \boldsymbol{H}\boldsymbol{\alpha}$, in which $\boldsymbol{H} \in \mathbb{R}^{n_S \times n_R}$ denotes the transition matrix from the mesh Σ to the mesh Ξ, defined componentwise as $h_{ij} = \mathcal{R}(\|\widetilde{\boldsymbol{\xi}}^{(i)} - \boldsymbol{\xi}^{(j)}\|)$, $i = 1, \ldots, n_S$, $j = 1, \ldots, n_R$. Aiming to keep the optimization process efficient, we assume that $n_R \leq n_S$. In specific, if $\Sigma = \Xi$, then $\boldsymbol{s}^\Sigma = \boldsymbol{G}\boldsymbol{\alpha}$.

Regarding the velocity field, it is obtained as the solution of problem (16) (or (17)) on the mesh Ξ. Then, in case $\Sigma \subset \Xi$, the components of $\boldsymbol{v}^\Sigma$, required for updating the parameters through equations (27)–(28), may be directly extracted from $\boldsymbol{v}^\Xi$. Otherwise, the RBFs may be used as interpolation functions to transfer not only the level set values, but also the sensitivities between the parameterization mesh and the FEM mesh (see e.g. [37]).

For the experiments with the *natural extension* of the velocity field, cf. Subsection 6.5, an approximate reinitialization scheme is adopted, following [36, 37]. The PLSF s is reescaled as

$$s_{\mathsf{re}}(\boldsymbol{x}, t) := \frac{s(\boldsymbol{x}, t)}{mean(\|\nabla\phi(\boldsymbol{x}^{(1)})\|, \ldots, \|\nabla\phi(\boldsymbol{x}^{(r)})\|)}, \tag{30}$$

in which $\boldsymbol{x}^{(i)}$, $i = 1, \ldots, r$ are the discretization knots around the zero level set, *mean* denotes

the arithmetic mean and $\|\cdot\|$ denotes the Euclidean norm. Due to the linear relationship between s and $\boldsymbol{\alpha}$, cf. eq. (23), it follows that $s_{\mathsf{re}}(\boldsymbol{x}, t) = \boldsymbol{r}(\boldsymbol{x})^{\mathsf{T}}\boldsymbol{\alpha}_{\mathsf{re}}(t)$, with

$$\boldsymbol{\alpha}_{\mathsf{re}}(t) := \frac{\boldsymbol{\alpha}(t)}{mean(\|\nabla\phi(\boldsymbol{x}^{(1)})\|, \ldots, \|\nabla\phi(\boldsymbol{x}^{(r)})\|)}. \tag{31}$$

The employed optimization scheme is summarized in Algorithm 1.

Algorithm 1: Parameterized level-set (PLS) topology optimization algorithm

---

Input: Parameterization mesh Σ, finite element mesh Ξ, prescribed volume fraction $\overline{V}$, initial Lagrange multiplier Λ_0, initial penalty parameter ρ_0, and updating parameters.

Initialize nodal values of the level-set function on the mesh Σ.

Solve interpolation problem for initial coefficients $\boldsymbol{\alpha}^{(0)}$.

while *stopping condition is not satisfied* **do**

> **Step 1:** Obtain an explicit representation of Ω^k on the mesh Ξ from $\boldsymbol{s}_{\Xi}^{(k)} = \boldsymbol{H}\boldsymbol{\alpha}^{(k)}$.
>
> **Step 2:** Solve the linear elasticity system (1) for Ω^k and evaluate the cost functional $\mathcal{L}_{\rho_k}(\Omega^k, \Lambda_k)$.
>
> **Step 3:** Solve the variational problem (16) (or (21)), to obtain the velocity field v_n (or $\boldsymbol{v}$) on Ξ.
>
> Convert the obtained velocity field to the mesh Σ.
>
> **Step 4:** Evolve $\boldsymbol{\alpha}^{(k+1)}$ according with equation (28) (or an analogous version based on (11)).
>
> If necessary, apply approximate reinitialization, cf. (31).
>
> **Step 5:** Update the Lagrange multiplier Λ_{k+1} and the penalty parameter ρ_{k+1}.

end

---

6 Computational results

Algorithm 1 has been implemented in `Python` (version 3.8.5). The solutions of the PDEs of Steps 2 and 3 were obtained by means of the `FEniCS` project resources ([18], see also `https://FEniCSproject.org/`) – version 2019.2.0.dev0. The experiments were run in a DELL Inspiron 7460 notebook, Intel Core i7-7500U processor clocked at 2.70GHz, 16GB RAM (64-bit). For the sparse matrix operations, the library `scipy` was used, together with the `umfpack` routines for linear systems. The code may be accessed at `https://github.com/giovannacandrade/RBF-Topology-Optimization`.

This section is organized as follows. We start by presenting the features of the test problems; the parameter choices; the details about the stopping conditions, the choice of the time step, and the initialization. In the first experiment, we discuss the effect of the extension-regularization parameter on the velocity field obtained by the *Hilbertian extension approach* and the particularities of its association with the parameterized level-set strategy. Then, the number of basis functions considered to parameterize the LSF is explored along with the finite element mesh refinement and, for a fixed pair of discretizations, the effect of the radius of support of the C2-Wendland basis functions is investigated. Next, the dependence on the

(a) Cantilever beam 1, $\overline{V} = 0.5$ [36].

(b) Cantilever beam 2, $\overline{V} = 0.4$, [7, 29].

(c) Bridge, $\overline{V} = 0.3$ [7].

(d) Half wheel, $\overline{V} = 0.3$ [29].

(e) MBB beam, $\overline{V} = 0.5$ [36, 29].
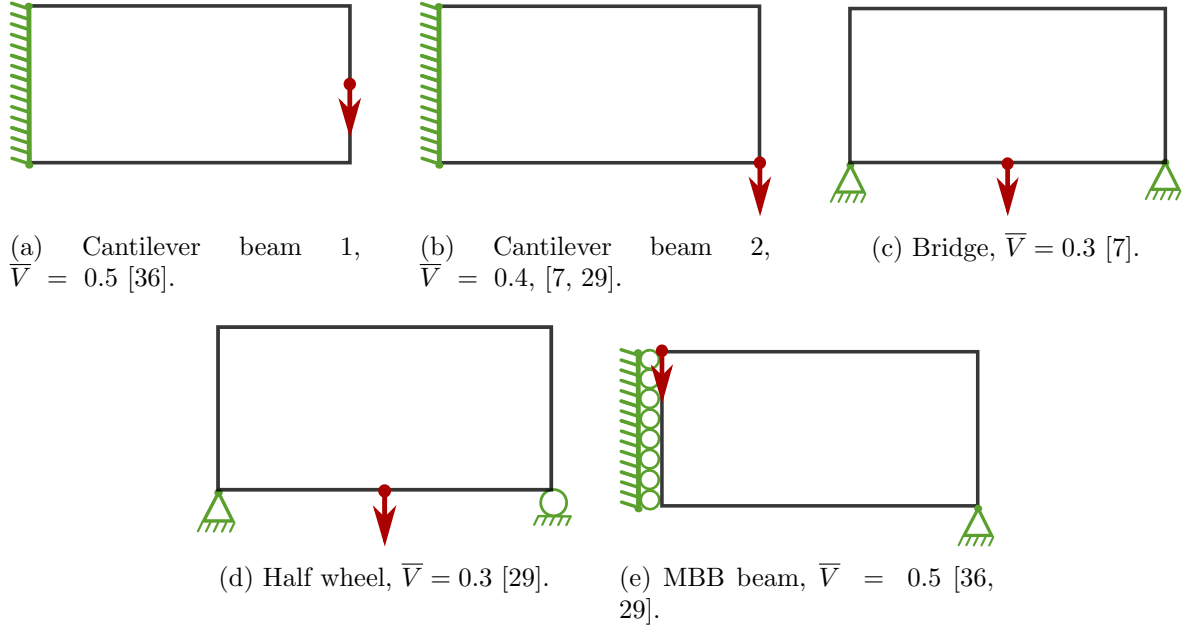
Figure 5: Benchmark test problems considered and respective prescribed volume fractions.

initial design and the possibility of hole nucleation are analyzed. Lastly, we experiment with different strategies for the extension of the velocity field, namely, the Hilbertian extension with volume expression of shape derivatives and the natural extension.

6.1 Main parameters

As benchmark test-problems, we consider two *cantilever beams* (differing by the position of the application of the force), a *bridge*, the *half wheel*, and the *MBB beam*. For the latter, the symmetry is exploited and only half of the beam is modeled. The corresponding boundary conditions and the prescribed fraction of volumes are provided in Figure 5, with the assumption that the traction forces are unitary. All working domains $\mathcal{D}$ were considered to be rectangular with normalized dimensions $l_x = 2$ and $l_y = 1$. The basis functions are assumed to be distributed on a structured rectangular mesh, denoted as *parameterization mesh*, with $n_x^R \times n_y^R$ elements of size h_R. As for the *finite element mesh*, we consider $n_x^S \times n_y^S$ elements of size h_S. The former is assumed to be contained in the latter, that is, $n_x^S/n_x^R = \ell$, with $\ell \in \mathbb{N}$.

The material's Young modulus and Poisson's ratio were set to $E = 1$ and $\nu = 0.3$, and the constant $\varepsilon = 10^{-9}$ was considered for the Ersatz material approach. The augmented Lagrangian parameters were determined heuristically based on preliminary experiments, in which we perceived the need for more cautious adjustments than the choices suggested in [4]. The initial Lagrange multiplier and the penalty parameter were set to $\Lambda_0 = 60$ and $\rho_0 = 1$, respectively, and the updating parameters, to $\rho_{max} = 5 \times 10^3$, $\gamma = 1.2$ and $\tau = 0.9$. As for the stopping criterion, we have considered

$$|\mathcal{L}_{\rho_k}(\Omega^k, \Lambda_k) - \mathcal{L}_{\rho_q}(\Omega^q, \Lambda_q)| \leq \tau_{\mathcal{L}}|\mathcal{L}_{\rho_k}(\Omega^k, \Lambda_k)|, \qquad q = k - 6, \ldots, k - 1. \qquad (32)$$

12

In order to avoid premature stops, the fraction of volume was also controlled according to

$$|\mathcal{C}(\Omega^q)| < \tau_{\mathcal{C}}, \qquad q = k - 3, \ldots, k. \tag{33}$$

For the experiments with the *Hilbertian extension approach,* tolerances were set to $\tau_{\mathcal{L}} = h_S/2$ and $\tau_{\mathcal{C}} = h_S$, so that more accuracy is required for thinner meshes. Additionally, we have adopted the budget of 150 maximum iterations. For the experiments with the *natural extension approach,* improvement on convergence was not observed as the meshes were refined, as discussed in Subsection 6.5. Therefore, tolerance was kept fixed at the corresponding value for the intermediate mesh considered ($\tau_{\mathcal{L}} = 1/180$ and $\tau_{\mathcal{C}} = 1/90$). In this case, we have increased the budget of maximum iterations to 400. To guarantee that the CFL (Courant–Friedrichs–Lewy) condition is satisfied, the obtained velocity fields were normalized with the maximum norm, so that $\max |v_n| = 1$, and the time step, determined heuristically, was taken as

$$\Delta t = \min\{0.02, 0.95 h_R\}. \tag{34}$$

The level set was initialized as suggested by Wei et al. [36, §3.1], with an additional scaling factor to adjust to our design domain dimensions, as illustrated in Figure 6. For the geometry mapping, based on preliminary experimentation, the bandwidth of (29) was set to $\Delta = h_S$, and the integration on the domain and at its boundary were performed using `FEniCS` resources [18, Chapter 1].
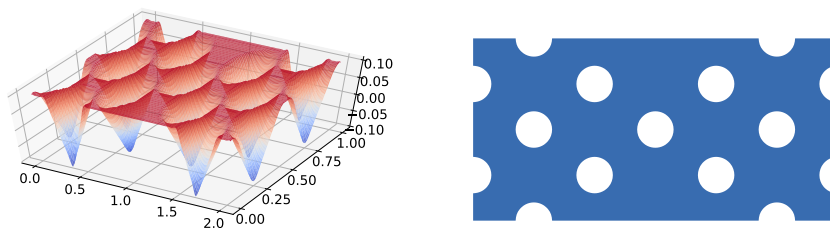
Figure 6: Graph of the initial level-set function and corresponding design domain.

6.2 The extension-regularization parameter of the boundary expression for the Hilbertian velocity extension

By adopting a Cartesian grid for the LSF discrete representation, most of its points will not lie at the interface [23]. Therefore, a proper velocity field should have its significant portion extended to at least a band around the boundary of the domain so that it can be captured by the nodes in which the PLSF is evolved. When working with the *Hilbertian extension approach,* this control can be done through the choice of the inner product (17), more specifically, by means of the *extension-regularization* parameter. In Figure 7 we present the velocity fields obtained with $a^2 = 1.25 \times 10^{-3}$, with parameterization mesh 60×30 and finite element mesh 180×90, overlapped by the current boundary of the design domain.

In the context of *conventional level-set methods,* some authors claim that the extension-regularization parameter should have the order of the element size, which would result in a less extended field as the mesh is refined [1]. Indeed, in Table 1, by zooming the upper-left portion of the first frame of Figure 7, and providing additional discretizations for both meshes, we illustrate the effect of resting just upon h_S to define a. For a fixed parameterization
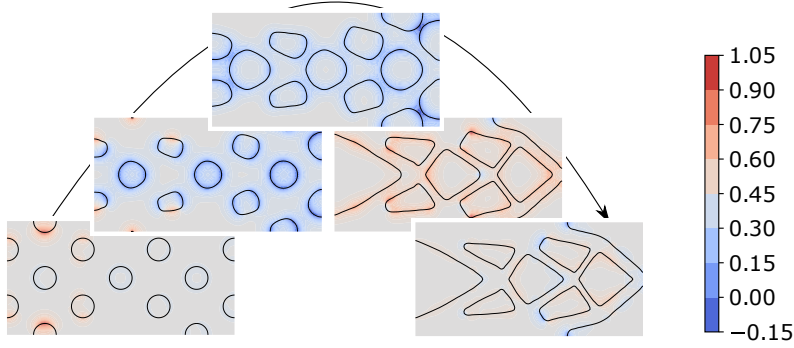
Figure 7: Evolution of the normalized velocity field, together with the boundary of the current design domain. The five frames correspond to iterations 1, 10, 20, 40, and 55 (convergence detected), respectively.

mesh, the significant portion of the velocity field would become more unapproachable by the parameterization knots as the finite element mesh is refined, impairing the expected evolution.

It should be noted that for the current work, since the finite element mesh is assumed to be decoupled from the parameterization mesh, although the variational problem (16) (or (21)) is solved on the former, the evolution scheme considers its values only on the latter, according with equations (27) and (28). Hence, we propose a choice for such parameter that takes into account both meshes, namely $a^2 := \min\{a^2_{\mathsf{max}}, \max\{a^2_{\mathsf{MG}}, a^2_{\mathsf{min}}\}\}$, in which $a_{\mathsf{MG}} := 2\sqrt{h_S h_R}$ is proportional to the geometric mean between the mesh sizes, and $a^2_{\mathsf{min}} = 7.5\times10^{-4}$, $a^2_{\mathsf{max}} = 1.25 \times 10^{-3}$ are lower and upper bounds heuristically determined. With the proposed choice, the aforementioned negative effect is alleviated.
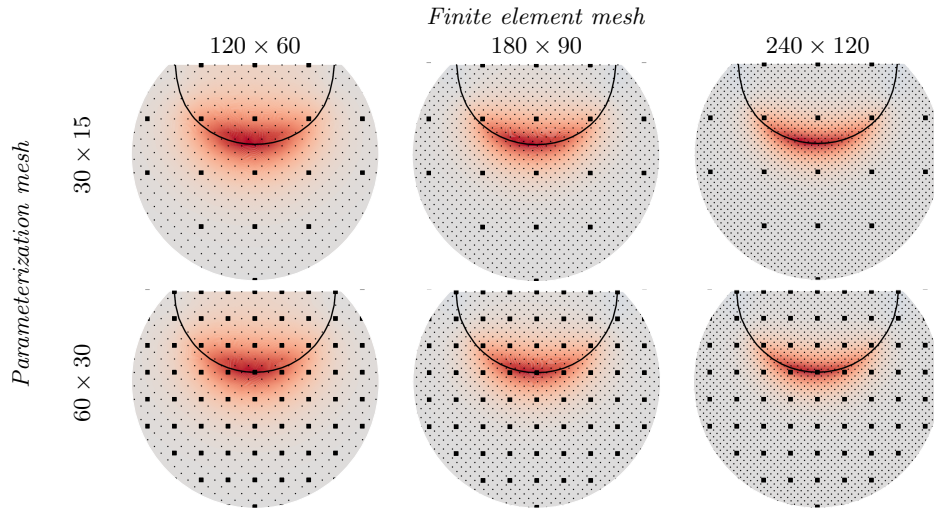
Table 1: Illustration of the negative effect of taking only h_S into account on the choice of the *extension-regularization* parameter. The darker knots represent the parameterization mesh, whereas the lighter ones correspond to the finite element mesh.

	Finite element mesh		
	120×60	180×90	240×120
Parameterization mesh 30×15	43 iterations	51 iterations	52 iterations
Parameterization mesh 60×30	48 iterations	55 iterations	61 iterations

Table 2: Final attained designs for *cantilever beam 1* and demanded number of iterations with the combined variations of mesh sizes.
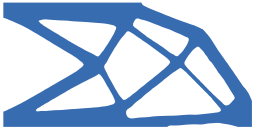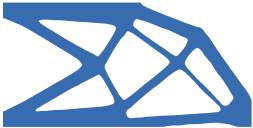
	Finite element mesh		
	120×60	180×90	240×120
Parameterization mesh 30×15	59 iterations	150 iterations(*)	150 iterations(*)
Parameterization mesh 60×30	66 iterations	71 iterations	101 iterations

Table 3: Final attained designs for *cantilever beam 2* and demanded number of iterations with the combined variations of mesh sizes – (*): the budget of maximum iterations is reached.

6.3 Assessing features of the radial basis functions

The quantity and the distribution of the basis functions are crucial aspects of a parameterized level set method. In computational terms, associating a basis function to each finite element knot, that is, adopting the same mesh for all the discretizations, may avoid intermediate steps and transition schemes. On the other hand, with decoupled meshes, it might be possible to meet the desired accuracy on the finite element analysis, while avoiding large-scale linear systems. To investigate this issue, we consider three finite element meshes and two parameterization meshes and evaluate the effects of each combination. To reduce other influences, for this experiment, all basis functions are identical, with a radius of support equivalent to 2.5 times the element size of the less refined parameterization mesh under consideration. The final designs obtained are presented in Tables 2–6, together with the number of performed iterations.

For the less refined parameterization mesh, it is possible to notice some difficulty in representing the boundary of the domain, especially associated with thin bars and leading to a lack of convergence in the case of the *cantilever beam 2* (cf. Table 3) and the *half wheel* (cf.

Table 4: Final attained designs for the *half-wheel* and demanded number of iterations with the combined variations of mesh sizes – (*): the budget of maximum iterations is reached.

Table 5: Final attained designs for the *bridge* and demanded number of iterations with the combined variations of mesh sizes.

Table 6: Final attained designs for the *MBB beam* and demanded number of iterations with the combined variations of mesh sizes.
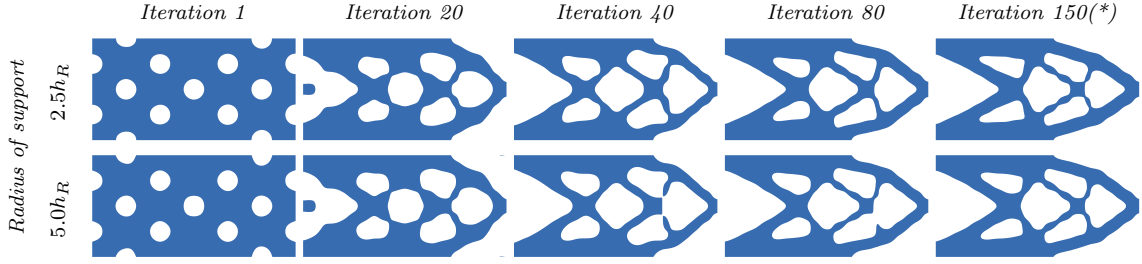
Table 7: Evolution of the design domain with two choices for the radius of support (finite element mesh 180×90 and parameterized mesh 20×10) – (*): the budget of maximum iterations is reached.

Table 4). Moreover, structural discontinuities can be observed in position (1,1) of Table 3, whereas structural asymmetry arises in positions (1,2) and (1,3) of Table 4. We attribute both effects to the use of too few basis functions. Indeed, to provide further evidence along this line, we have considered a 20×10 parameterization mesh and exhibit, for the *cantilever beam 1,* the evolution process for two radii of support in Table 7. Indeed, although the same topology of Table 2 is maintained, the irregularities associated with thin bars are enhanced and the effect is not relieved when the CS-RBF support ratio is increased, indicating that the difficulty can be attributed to the use of too few basis functions. In [37], the authors ran a similar experiment, with an unstructured finite element mesh, and a comparable instability was observed, also leading to a different topology in the case of the 20×10 parameterization mesh.

For fixed parameterization and finite element meshes, we have investigated the effect of the radius of support of the CS-RBF as well. The final obtained designs are presented in Table 8. For the smallest radius of support, irregular boundaries are obtained, leading also to modifications to the final design, especially in the case of the *cantilever beam 2*, the *half wheel*, and the *MBB beam*. The occurrence of unconnected regions can be associated with a difficulty similar to the one illustrated in Figure 7. For the remaining investigated choices, the final obtained designs are similar and have smooth boundaries.

The CPU time per iteration for each case is presented in Figure 8. The tendency of growth as the radius of support is enlarged can be attributed to the expansion of the bandwidth of the associated matrices, as illustrated in the first row of Table 8. A similar experiment is presented in [20] for compliant mechanisms. For the largest radius of support, a different structure was obtained, which, according to the authors, can be attributed to a strong diffusion term. Therefore, for a good trade-off between computational effort and capability of representing well the level set function, a support radius of $d_{sp} = 2.5h_R$ is considered for the experiments that come in the sequel.
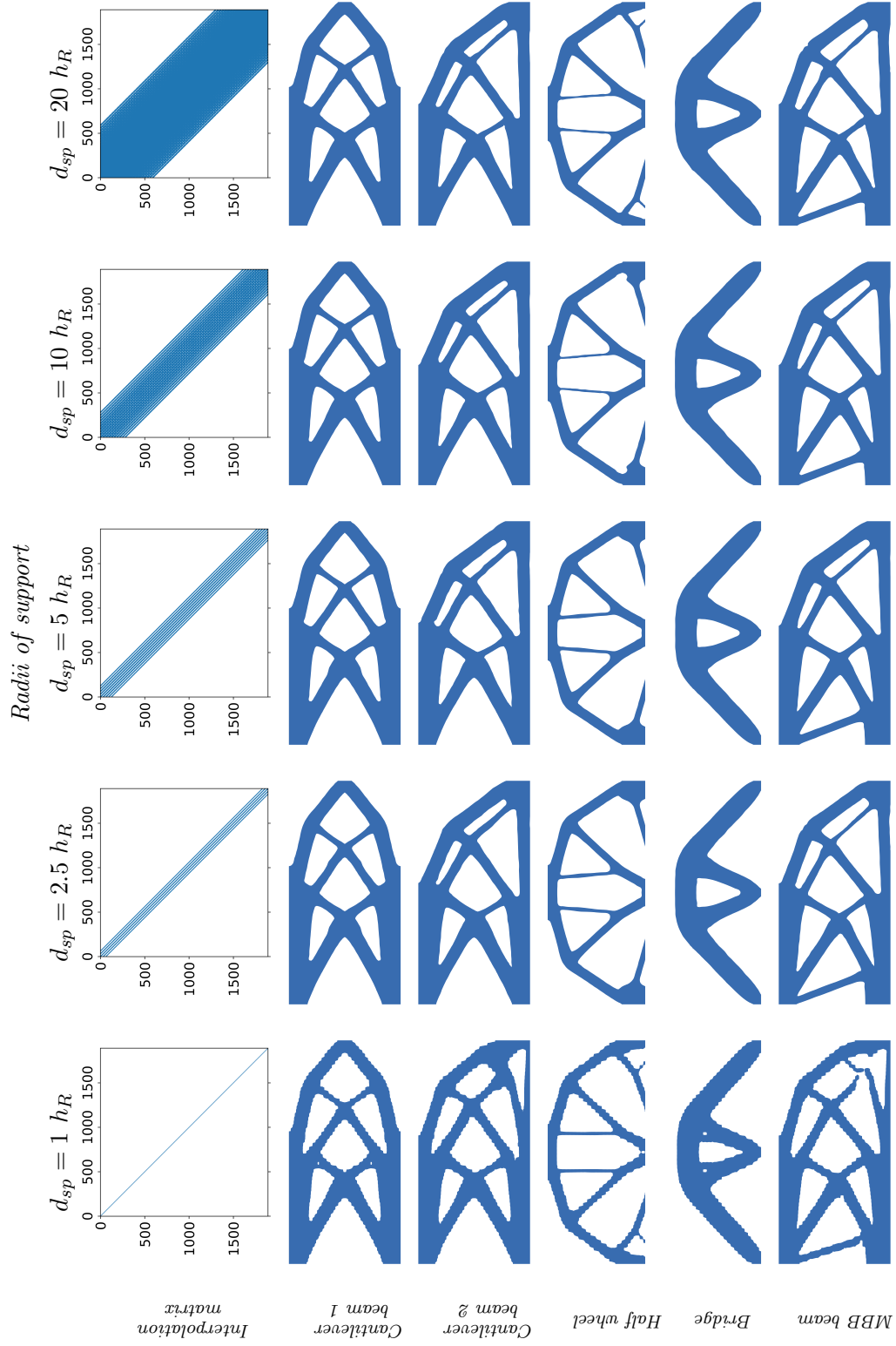
Table 8: Interpolation matrices and attained structures for each test problem and the distinct radii of support (finite element mesh 180×90, and parameterization mesh 60×30).
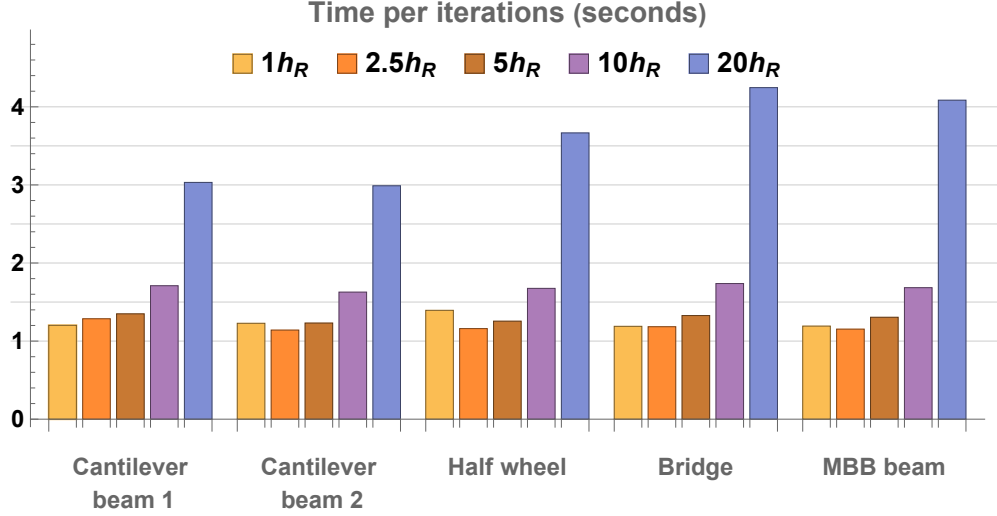
Figure 8: CPU time per iteration for each test problem and the distinct radii of support.

6.4 Influence of the initial configuration

Dependency on the initial configuration is a classical issue in structural optimization [32]. It is known that in its general continuous setting, sine the space of admissible sets is not closed, the compliance minimization problem suffers from the lack of existence of a solution [3]. Although the discrete version of the problem usually admits global minimizers, the aforementioned problematic implies, in general, that the solutions are related to the chosen refinement. A mesh-independent algorithm also depends on hole nucleation, that is, on the ability to create new holes. In *conventional level set methods*, however, solving the Hamilton-Jacobi equation under a strict condition for numerical stability or adopting reinitialization schemes inhibits the occurrence of nucleation [6].

When it comes to the parameterized level set approach with radial basis functions, the possibility of nucleation has been identified in the literature due to the capability of (a) maintaining the smoothness of the level set function without adopting reinitialization schemes, cf. [35]; (b) seeking for an approximate solution of the HJ partial differential equation, cf. [34], and (c) adopting the *natural extension approach*, cf. [36]. Indeed, according to Dijk et al. [32], the natural velocity extension can lead to hole nucleation, but it is an accidental phenomenon.

With the strategy under consideration, no explicit hole nucleation mechanism is incorporated, and some dependence on the initial guess is expected. With the consistent updating procedure proposed, we aim to investigate the actual potential of nucleation of the Hilbertian extension of the velocity field combined with the CS-RBF parameterization. To accomplish this task, we consider five distinct initial domains, with different numbers of initial holes, exhibited in Table 9. Except for case (i), in which the initial PLSF is defined as zero on the reference boundary domain, and 0.1 on its interior, the initial configurations are defined similarly to the one presented in Figure 6, just varying the number, the distribution and the radius of the initial holes. Indeed, the results show that final designs with more internal holes are usually obtained as the number of initial holes increases, indicating that the algorithm is

19

capable of merging holes, but not creating new ones. On the other hand, when the magnitude of ϕ for the experiment (i) is altered, nucleation is observed, as presented in Table 10. The phenomenon can be considered an accidental effect caused by the combination of the strategy of geometry mapping and the Hilbertian extension approach.
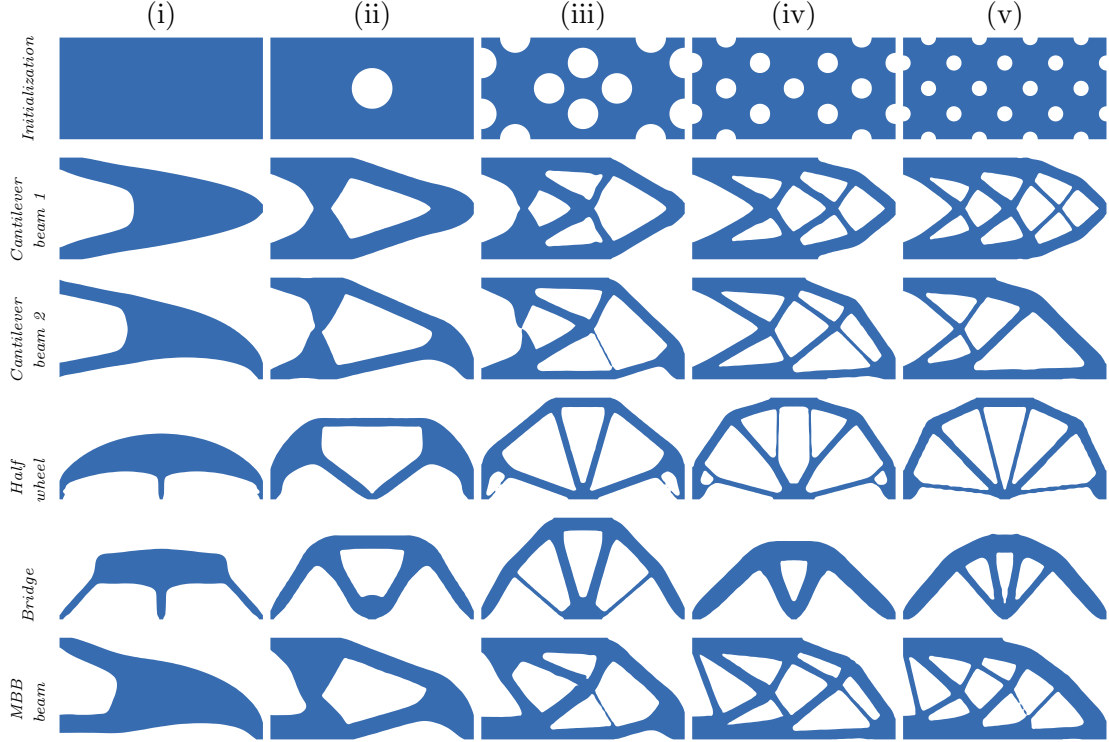

Table 9: Final design obtained for different initial configurations, for each test-problem (finite element mesh 180×90, and parameterization mesh 60×30).
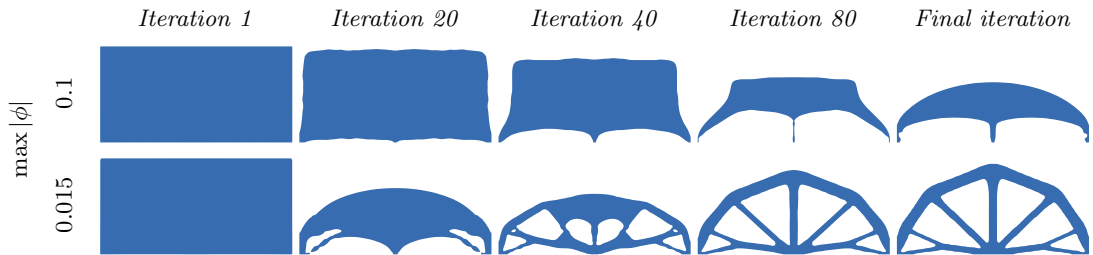

Table 10: Evolution of the design domain for the half wheel with two distinct initializations for the LSF. Finite element mesh 180×90, and parameterization mesh 60×30. Convergence at iteration 143 (top), and reaching the budget of maximum 150 iterations (bottom).

6.5 Velocity field extension

For this experiment, we contrast the proposed strategy with two alternative approaches for obtaining and extending the velocity field (Step 3 of Algorithm 1). Firstly, we consider the

Hilbertian extension approach with volume expression of shape derivative, cf. eqs. (20)–(22), and evolution equation based on (11). Secondly, we consider the *natural extension approach,* along with the modified HJ equation (13). For this choice, the velocity field is obtained by integrating the expression (15) over each element, which is similar to the strategy adopted by [36]. For the *natural extension approach,* to prevent the level set function from becoming too flat or too steep, the approximate reinitialization scheme defined in the end of Section 5 was adopted [36]. For a fixed parameterization mesh of 60×30, the final designs obtained for the cantilever beam 1 with each strategy and different FEM meshes are presented in Table 11.

For the experiment with volume expression of the shape derivative, the time step was defined as in (34) and the extension-regularization parameter adopted for the inner product (22) was the same as discussed in Subsection 6.2. As for the time step on the *natural extension approach*, we experiment first with a choice similar to [36], which consists in normalizing the velocity field with its median and taking a fixed time step of $\Delta t = 5 \times 10^{-3}$. Nevertheless, with this choice, the CFL condition is not satisfied, and a direct comparison with the former experiments is difficult. Indeed, in [34], the authors discussed that, by seeking approximate solutions to the PDE, the CFL condition can be relaxed with the RBF-parameterized approach. However, considering that one of the goals of this work is to isolate and systematically analyze different aspects of the solution approaches, we avoid introducing further approximation errors.

Therefore, aiming to contrast approaches under similar conditions, we experiment with the combination of the *natural extension approach* and the time step given by (34). As depicted in Table 11, with this choice we have obtained a very large number of iterations, which is consistent with the observation of de Gournay [11] regarding the convergence speed of the Hilbertian extension in contrast with the natural extension. Moreover, unsatisfactory final designs were obtained. We recognize, however, that due to the drastic change of behavior, the augmented Lagrangian parameters may not be well calibrated for this choice. Furthermore, we experiment with adopting 10 steps of size (34) for each velocity field, which is a heuristic attempt of accelerating the process, and the experiments presented in the sequel were performed with this choice.

The evolution of the objective function, compliance, fraction of volume and augmented Lagrangian parameters for the first, second and last experiments of Table 11 are presented in Table 12. Also, for a fixed refinement of 180×90 for the FEM mesh, the level set functions obtained for each case are presented in Figure 9. Results have shown that the *natural extension approach* offers more dependency on the chosen mesh and the outcomes are not necessarily improved as the finite element mesh is refined, which goes against the expected improvement in accuracy. As for the final surfaces, with the combination of the Hilbertian extension of shape derivative with the RBF parameterization and evolution equation (13), no unbounded growth of the PLSF was observed. Indeed, without adopting any reinitialization strategy, the magnitude of ϕ was kept as in the initial configuration depicted in Figure 6.

7   Final remarks

Summarizing the main aspects which emerged from our numerical investigation, the first comment concerns the extension-regularization parameter a of the Hilbertian extension. It controls the spreading of the velocity field from the boundary of the current design domain,

	120×60	180×90	240×120
Hilbertian Extension (eq. (15))	48 iterations	55 iterations	60 iterations
Hilbertian Extension (eq. (20))	47 iterations	49 iterations	57 iterations
Natural Extension cf. Wei et al. [36]	26 iterations	26 iterations	24 iterations
Natural Extension (Δt cf. eq. (34))	149 iterations	238 iterations	400 iterations(*)
Natural Extension (*10 inner its. - Δt cf. eq. (34)*)	41 iterations	52 iterations	76 iterations

Table 11: Final designs obtained for the *cantilever beam 1* with distinct choices for the velocity extension, with parameterization mesh 60×30 and three different refinements for the finite element mesh – (*): the budget of maximum iterations is reached.

and we have noticed a high sensitivity of the results with very small variations of a, to the extent of impairing the convergence of the generated sequence of approximations to the solution. Moreover, since we have allowed decoupling between the parameterization and the finite element meshes, it turned out to be essential to ensure that the velocity extension encompasses a strip containing a significant number of nodes of the mesh in charge of the evolution of the LSF.

Second, we should stress the possibility of employing a smaller number of compactly supported RBFs in comparison with the number of nodes of the finite element mesh. As a result, the used matrices may become even more sparse. Nevertheless, with a very reduced number of basis functions, the design domain might be poorly represented, spoiling the effectiveness of the parameterization strategy.

Third, regarding the dependence of the results concerning the initial configuration and the refinement of the mesh, we did not observe the occurrence of systematic nucleation. The new holes that eventually appeared in our results may be associated with small values for the
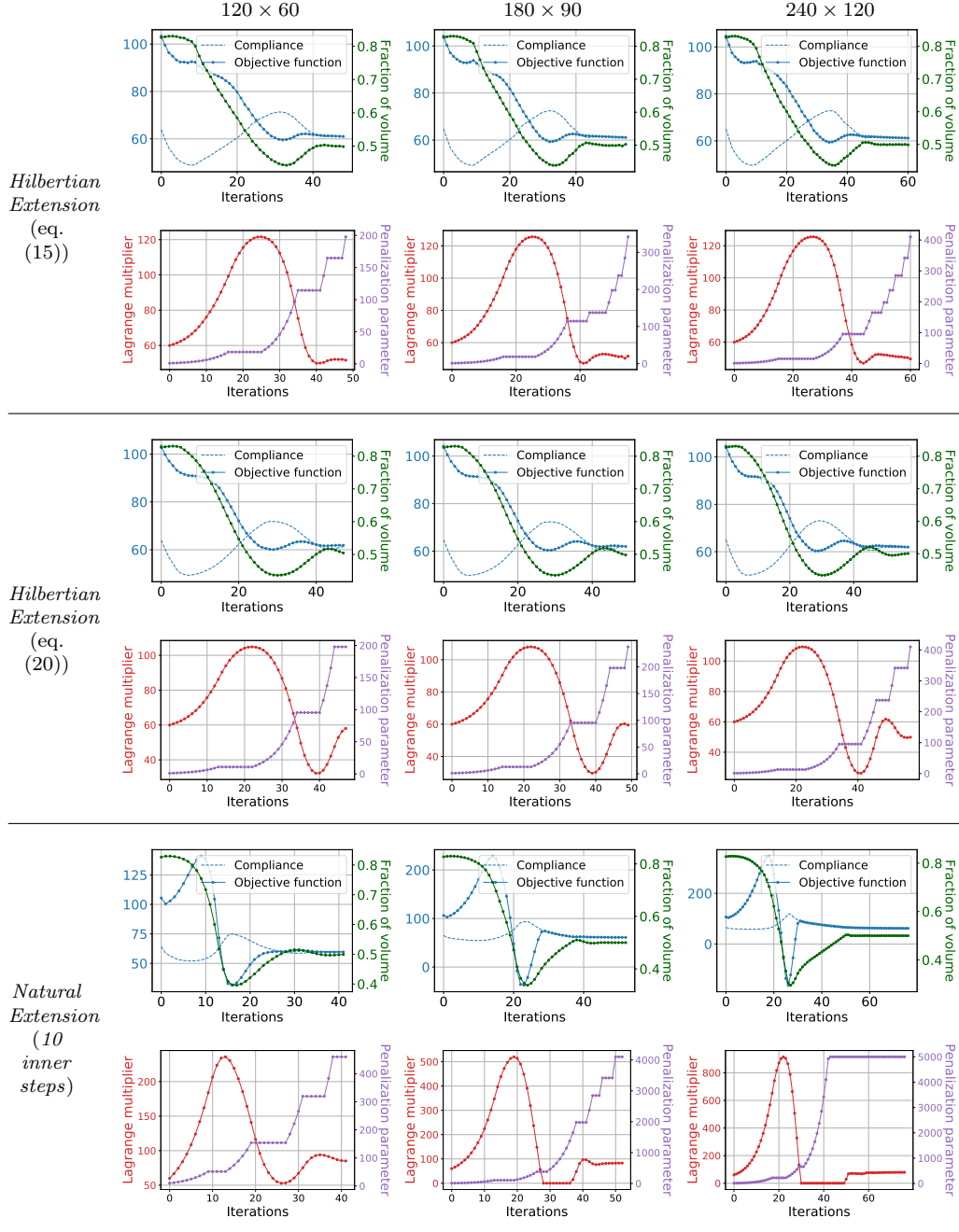
Table 12: Evolution curves corresponding to the instances of the first (top), second (middle) and last (bottom) rows of Table 11.
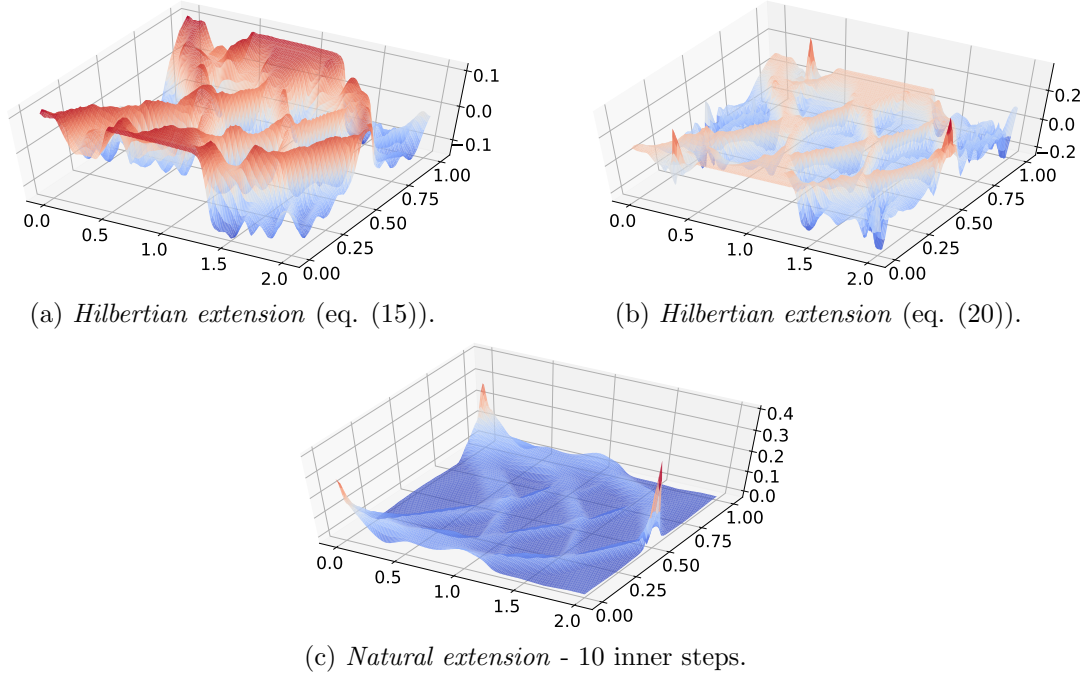
(a) *Hilbertian extension* (eq. (15)).

(b) *Hilbertian extension* (eq. (20)).

(c) *Natural extension* - 10 inner steps.

Figure 9: Final LSF surface graphs for the three instances of Table 12 with finite element mesh 180×90.

initial LSF. Among the policies that may ensure nucleation we should refer to modifications in the Hamilton-Jacobi equation, with additional reaction-diffusion terms that encompass topological derivatives (see e.g. [7, 26, 39, 14, 9, 10]).

Last but not least, it is worth mentioning that our results with the Hilbertian extension were less dependent on the mesh than the results with the natural extension. Such a behavior provided further support for our goal of analyzing the influence of the combined parameters and the several elements in the most isolated way possible.

All in all, our study revealed the potentiality of parameterized LSFs based on compactly supported RBFs, together with a Hilbertian extension of the velocity and the modified Hamilton-Jacobi equation (13) in maintaining a sufficiently smooth and bounded function, without any reinitialization strategy, for solving compliance minimization problems. By tackling the possibility of decoupling the finite element nodes from the design variables stated by the RBF parameterization, we believe to have pointed out a worthy framework to address, for instance, symmetry and pattern repetition constraints, and also unstructured meshes (see e.g. [17, 16] and references therein). Possible topics for future investigation include a further study of the theoretical aspects concerning the convergence analysis of the proposed scheme, as well as the inherent error associated with the usage of the modified Hamilton-Jacobi equations.

comments that improved the presentation of the text

References

[1] G. Allaire, C. Dapogny, G. Delgado, and G. Michailidis. Multi-phase structural optimization via a level set method. *ESAIM: Control, Optimisation and Calculus of Variations*, 20:576–611, 2014.

[2] G. Allaire, F. Jouve, and A.-M. Toader. Structural optimization using sensitivity analysis and a level-set method. *Journal of Computational Physics*, 194:363–393, 2004.

[3] M. P. Bendsøe and O. Sigmund. *Topology Optimization: Theory, Methods, and Applications*. Engineering online library. Springer, Berlin Heidelberg, 2003.

[4] E. G. Birgin and J. M. Martínez. *Practical Augmented Lagrangian Methods for Constrained Optimization*. SIAM, Philadelphia, USA, 2014.

[5] M. D. Buhmann. *Radial Basis Functions: Theory and Implementations*. Cambridge Monographs on Applied and Computational Mathematics. Cambridge University Press, Cambridge, 2003.

[6] M. Burger and S. J. Osher. A survey on level set methods for inverse problems and optimal design. *European Journal of Applied Mathematics*, 16(2):263–301, 2005.

[7] V. J. Challis. A discrete level-set topology optimization code written in Matlab. *Structural and Multidisciplinary Optimization*, 41(3):453–464, 2010.

[8] Z. Chen. *Finite Element Methods and Their Applications*. Springer, Berlin Heidelberg, 2005.

[9] M. Cui, H. Chen, and J. Zhou. A level-set based multi-material topology optimization method using a reaction diffusion equation. *Computer-Aided Design*, 73:41–52, 2016.

[10] M. Cui, M. Pan, J. Wang, and P. Li. A parameterized level set method for structural topology optimization based on reaction diffusion equation and fuzzy PID control algorithm. *Electronic Research Archive*, 30(7):2568–2599, 2022.

[11] F. de Gournay. Velocity extension for the level-set method and multiple eigenvalues in shape optimization. *SIAM Journal on Control and Optimization*, 45(1):343–367, 2006.

[12] J. D. Deaton and R. V. Grandhi. A survey of structural and multidisciplinary continuum topology optimization: post 2000. *Structural and Multidisciplinary Optimization*, 49:1–38, 2014.

[13] M. C. Delfour and J.-P. Zolésio. *Shapes and Geometries: Metrics, Analysis, Differential Calculus, and Optimization*. Society for Industrial and Applied Mathematics, Philadelphia, 2d edition, 2011.

[14] C. Kim, M. Jung, T. Yamada, S. Nishiwaki, and J. Yoo. Freefem++ code for reaction-diffusion equation–based topology optimization: for high-resolution boundary representation using adaptive mesh refinement. *Structural and Multidisciplinary Optimization*, 62, 02 2020.

[15] A. Laurain. A level set-based structural optimization code using FEniCS. *Structural and Multidisciplinary Optimization*, 58(3):1311–1334, 2018.

[16] H. Lin, H. Liu, and P. Wei. A parallel parameterized level set topology optimization framework for large-scale structures with unstructured meshes. *Computer Methods in Applied Mechanics and Engineering*, 397:115112, 2022.

[17] Y. Liu, Z. Li, P. Wei, and W. Wang. Parameterized level-set based topology optimization method considering symmetry and pattern repetition constraints. *Computer Methods in Applied Mechanics and Engineering*, 340:1079–1101, 2018.

[18] A. Logg, K.-A. Mardal, and G. N. Wells. *Automated Solution of Differential Equations by the Finite Element Method - The FEniCS Book.* Lecture Notes in Computational Science and Engineering (LNCSE, volume 84). Springer-Verlag, Berlin Heidelberg, 2012.

[19] D. Luenberger. *Optimization by Vector Space Methods.* Professional Series. Wiley, New York, 1969.

[20] Z. Luo, L. Tong, M. Y. Wang, and S. Wang. Shape and topology optimization of compliant mechanisms using a parameterization level set method. *Journal of Computational Physics,* 227(1):680–705, 2007.

[21] M. Cui, C. Luo, G. Li, and M. Pan. The parameterized level set method for structural topology optimization with shape sensitivity constraint factor. *Engineering with Computers,* 37:855–872, 2021.

[22] J. Nocedal and S. J. Wright. *Numerical Optimization.* Springer, New York, NY, USA, second edition, 2006.

[23] S. Osher and R. Fedkiw. *Level Set Methods and Dynamic Implicit Surfaces.* Springer, New York, 2003.

[24] S. Osher and R. P. Fedkiw. Level Set Methods: An Overview and Some Recent Results. *Journal of Computational Physics,* 169(2):463–502, 2001.

[25] S. Osher and J. A. Sethian. Fronts propagating with curvature-dependent speed: Algorithms based on Hamilton-Jacobi formulations. *Journal of Computational Physics,* 79(1):12–49, 1988.

[26] M. Otomori, T. Yamada, K. Izui, and S. Nishiwaki. Matlab code for a level set-based topology optimization method using a reaction diffusion equation. *Structural and Multidisciplinary Optimization,* 51(5):1159–1172, 2015.

[27] J. N. Reddy. *An Introduction to Continuum Mechanics.* Cambridge University Press, 2nd edition, 2013.

[28] J. Sethian. *Level-Set Methods and Fast Marching Methods: Evolving Interfaces in Computational Geometry, Fluid Mechanics, Computer Vision and Materials Science.* Cambridge University Press, 2nd edition, 1999.

[29] O. Sigmund. A 99 line topology optimization code written in Matlab. *Structural and Multidisciplinary Optimization,* 21:120–127, 2001.

[30] O. Sigmund and K. Maute. Topology optimization approaches a comparative review. *Structural and Multidisciplinary Optimization,* 48(6):1031–1055, 2013.

[31] J. Sokolowski and J. Zolésio. *Introduction to Shape Optimization: Shape Sensitivity Analysis.* Lecture Notes in Computer Science. Springer, Berlin Heidelberg, 1992.

[32] N. P. Van Dijk, K. Maute, M. Langelaar, and F. Van Keulen. Level-set methods for structural topology optimization: a review. *Structural and Multidisciplinary Optimization,* 48(3):437–472, 2013.

[33] L. Wang, Z. Li, B. Ni, X. Wang, and W. Chen. A robust topology optimization method considering bounded field parameters with uncertainties based on the variable time step parametric level-set method. *Applied Mathematical Modelling,* 107:441–463, 2022.

[34] S. Wang, K. Lim, B. Khoo, and M. Wang. An extended level set method for shape and topology optimization. *Journal of Computational Physics,* 221(1):395–421, 2007.

[35] S. Wang and M. Y. Wang. Radial basis functions and level set method for structural topology optimization. *International Journal for Numerical Methods in Engineering,* 65(12):2060–2090, 2006.

[36] P. Wei, Z. Li, X. Li, and M. Y. Wang. An 88-line MATLAB code for the parameterized level set method based topology optimization using radial basis functions. *Structural and Multidisciplinary Optimization*, 58(2):831–849, 2018.

[37] P. Wei, Y. Yang, S. Chen, and M. Y. Wang. A Study on Basis Functions of the Parameterized Level Set Method for Topology Optimization of Continuums. *Journal of Mechanical Design*, 143(4):041701(1–17), 2021.

[38] H. Wendland. Piecewise polynomial, positive definite and compactly supported radial functions of minimal degree. *Advances in Computational Mathematics*, 4:389–396, 1995.

[39] T. Yamada, K. Izui, S. Nishiwaki, and A. Takezawa. A topology optimization method based on the level set method incorporating a fictitious interface energy. *Computer Methods in Applied Mechanics and Engineering*, 199(45):2876–2891, 2010.

[40] J. Zhu, H. Zhou, C. Wang, L. Zhou, S. Yuan, and W. Zhang. A review of topology optimization for additive manufacturing: Status and challenges. *Chinese Journal of Aeronautics*, 34(1):91–110, 2021.